Heterogeneous Memristive Devices Enabled by Magnetic Tunnel Junction Nanopillars Surrounded by Resistive Silicon Switches

Yu Zhang, Xiaoyang Lin, Jean-Paul Adam, Guillaume Agnus, Wang Kang, Wenlong Cai, Jean-Rene Coudevylle, Nathalie Isac, Jianlei Yang, Huaiwen Yang, Kaihua Cao, Hushan Cui, Deming Zhang, Youguang Zhang, Chao Zhao, Weisheng Zhao,* and Dafine Ravelosona

Emerging nonvolatile memories (NVMs) have currently attracted great interest for their potential applications in advanced low-power information storage and processing technologies. Conventional NVMs, such as magnetic random access memory and resistive random access memory, suffer from limitations of low tunnel magnetoresistance, low access speed, or finite endurance. NVMs with synergetic advantages are still highly desired for future computer architectures. This study reports a heterogeneous memristive device composed of a magnetic tunnel junction (MTJ) nanopillar surrounded by resistive silicon switches, named resistively enhanced MTJ (Re-MTJ), which may be utilized for novel memristive memories, enabling new functionalities that are inaccessible for conventional NVMs. The Re-MTJ device features a high ON/OFF ratio of >1000% and multilevel resistance behavior by combining magnetic switching together with resistive switching mechanisms. The magnetic switching originates from the MTJ, while the resistive switching is induced by a point-switching filament process that is related to the mobile oxygen ions. Microscopic evidence of silicon aggregated as nanocrystals along the edges of the nanopillars verifies the synergetic mechanism of the heterogeneous memristive device. This device may provide new possibilities for advanced memristive memory and computing architectures, e.g., in-memory computing and neuromorphics.

Y. Zhang, Dr. X. Lin, Dr. W. Kang, W. Cai, Dr. J. Yang,
Dr. H. Yang, K. Cao, H. Cui, Dr. D. Zhang, Prof. Y. G. Zhang,
Prof. C. Zhao, Prof. W. Zhao
Fert Beijing Institute
BDBC Beihang University
Beijing 100191, China
E-mail: weisheng.zhao@buaa.edu.cn
Y. Zhang, Dr. J.-P. Adam, Dr. G. Agnus, Dr. J.-R. Coudevylle, N. Isac,
Dr. D. Ravelosona
Centre de Nanosciences et de Nanotechnologies
University of Paris-Sud
Université Paris-Saclay
Orsay 91405, France
K. Cao, H. Cui, Prof. C. Zhao
Institute of Microelectronics
Chinese Academy of Sciences
Beijing 100029, China

1. Introduction

Nonvolatile memories (NVMs) combined with novel computing architectures have recently been considered as the most promising solution to overcome the "memory wall" of von-Neumann computing systems.[1–3] For instance, in-memory computing architectures based on closely integrating fast NVMs with logic functions have been proposed to minimize the power consumption and pave the way toward normally-off/ instant-on computing.[4,5] Meanwhile, neuromorphic computing inspired by the human brain exploits the resistive features of NVMs as artificial synapses and neurons and has already triggered a revolution for non-von-Neumann architectures.[6–8] Along this direction, two of the most promising NVMs, i.e., magnetic random access memory (MRAM)[3,9–11] and resistive random access memory (RRAM),[3,12–14] have attracted increasing interest. Tremendous efforts have been involved and amazing advances have been achieved in this field. Nevertheless, a few issues still exist and should be addressed before popular applications can be achieved. For example, multilevel resistance states can be achieved in either magnetic tunnel junctions (MTJs, the core device of MRAM) or RRAM devices. For MTJ devices, there are two main methods to obtain the multilevel resistance states, either by taking advantage of the stochastic behavior of the magnetic switching,[15] or by using vertical stacked MTJs as multilevel cell.[16] However, both of methods suffer from a challenge of a relative low tunnel magnetoresistance (TMR) ratio (<250% to date), which is a key limitation for high density and high reliability applications.[17–19] Regarding RRAM devices with high ON/OFF ratios, they can provide the perfect multilevel resistances required for applications, but its relative low access speed and endurance issues are limited by its intrinsic mechanism as electrochemical reduction and Joule heating process, which have become an intrinsic drawback for computing tasks.

Therefore, an NVM that eliminates these shortcomings, for example, by integrating MRAM and RRAM into a single device, is still highly desired. Several recent studies based on an MgO-based MTJ have exhibited both magnetic switching (MS) and resistive switching (RS), enabling such possibilities.[20–22] However, those devices suffer from a trade-off between MS and RS as the MgO layer acts as both a tunnel barrier for MS and an insulator for RS. In this work, we report a novel heterogeneous memristive device composed of an MTJ nanopillar surrounded by resistive silicon switches, named a resistively enhanced MTJ (Re-MTJ), which can combine the advantages of both RRAM and MRAM for realizing advanced memristive memories. Different from previous studies, the RS in our proposed Re-MTJ originates from a point-switching filament process related to the mobile oxygen ions,[23–26] while the MS from the MTJ. The MS and RS in the Re-MTJ can be individually optimized. Furthermore, our tests show that the Re-MTJ device can achieve a rather high ON/OFF ratio of >1000% and multilevel resistance behavior; both of these characteristics are urgently required in advanced NVMs. In addition, the Re-MTJ may provide new functionalities that are inaccessible to conventional NVMs, e.g., for in-memory computing and neuromorphic computing as non-von-Neumann computing architectures.

2. Results and Discussion

Figure 1a shows a schematic view of the Re-MTJ device made of an in-plane magnetized CoFe(B)-MgO MTJ nanopillar and a SiO$_x$-based polymer encapsulation layer. In the MTJ structure, the MgO tunnel barrier is sandwiched by two CoFe(B)-based magnetic thin films corresponding to the free and reference layers. Driven by either an in-plane magnetic field or a spin-polarized current, the MTJ can be switched between parallel (P) and antiparallel (AP) states, leading to two resistance states, namely, R_P and R_{AP}, respectively. Figure 1b shows a cross-sectional transmission electron microscope (TEM) image of the device. The Re-MTJ devices were fabricated in a method similar to the conventional MTJs. The magnetic films were patterned into submicrometer-sized ellipses with dimension ranging from 80×160 nm^2 to 100×240 nm^2 using electron beam lithography and an angle-optimized ion beam etching process. Then, the MTJ nanopillars were encapsulated by a Si-O-based insulator fabricated by baking a polymer (Accuflo)[27] at a reduced temperature. As shown in Figure 1c, the cross-sectional TEM image of MTJ stacks after annealing indicates the presence of the crystallized MgO tunnel barrier and CoFe(B) layers, which have been reported as NaCl-structure and body-centred cubic (bcc) structures, respectively.[9,28]

Figure 2 indicates the very peculiar resistive behavior of the device under an applied voltage resulting from the combination of current-induced magnetization switching (CIMS) and voltage-induced resistive switching (VIRS). Indeed, as shown in the typical $I–V$ curves of Figure 2a, bipolar (in which positive and negative voltages have opposite effects) VIRS was observed in the absence of external magnetic fields, with a maximum voltage of 0.8 V. For this measurement, the MTJ was
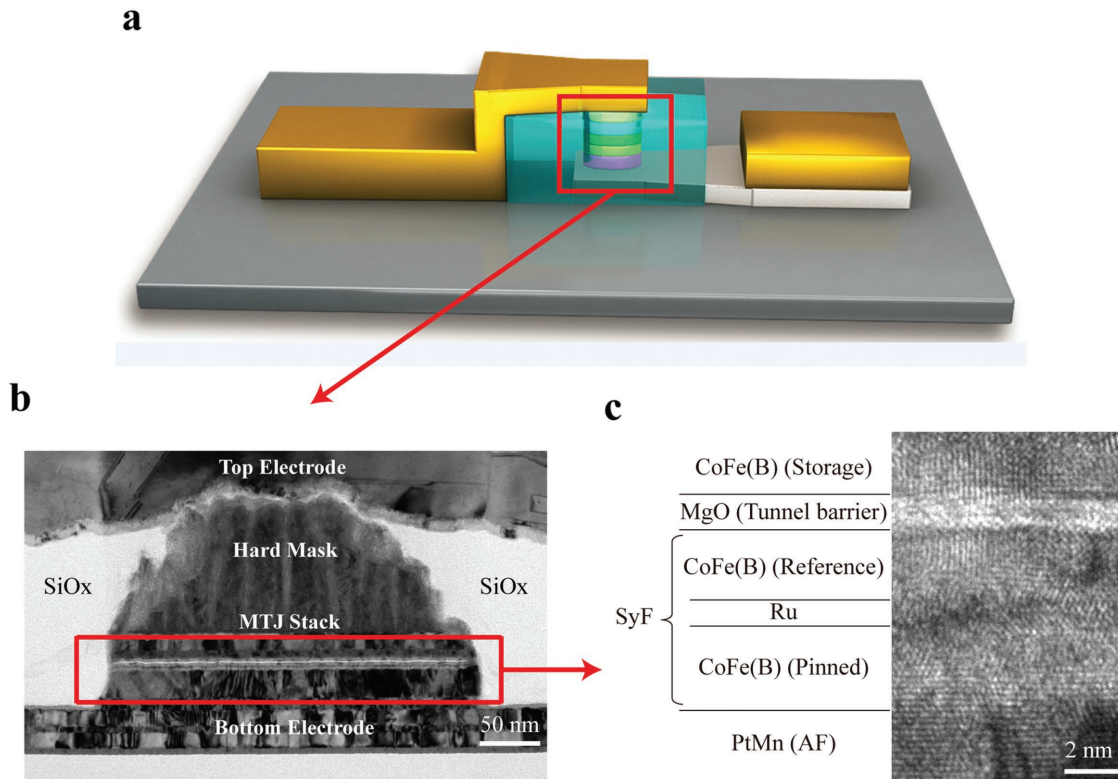

Figure 1. Re-MTJ device. a) Schematic of the Re-MTJ device. A two-terminal MTJ nanopillar is encapsulated within a SiO$_x$-based matrix. b) TEM image of the Re-MTJ device. The top electrode, hard mask, MTJ stack (indicated with a red rectangular), and bottom electrode are indicated. c) HRTEM image of a CoFe(B)-MgO-based MTJ nanopillar. The free layer (CoFe(B)), tunnel barrier (MgO), synthetic ferrimagnetic (SyF) reference layer (CoFe(B)/Ru/CoFe(B)), and anti-ferromagnetic layer PtMn are indicated. A crystalline structure can be observed for both CoFe(B) and MgO.
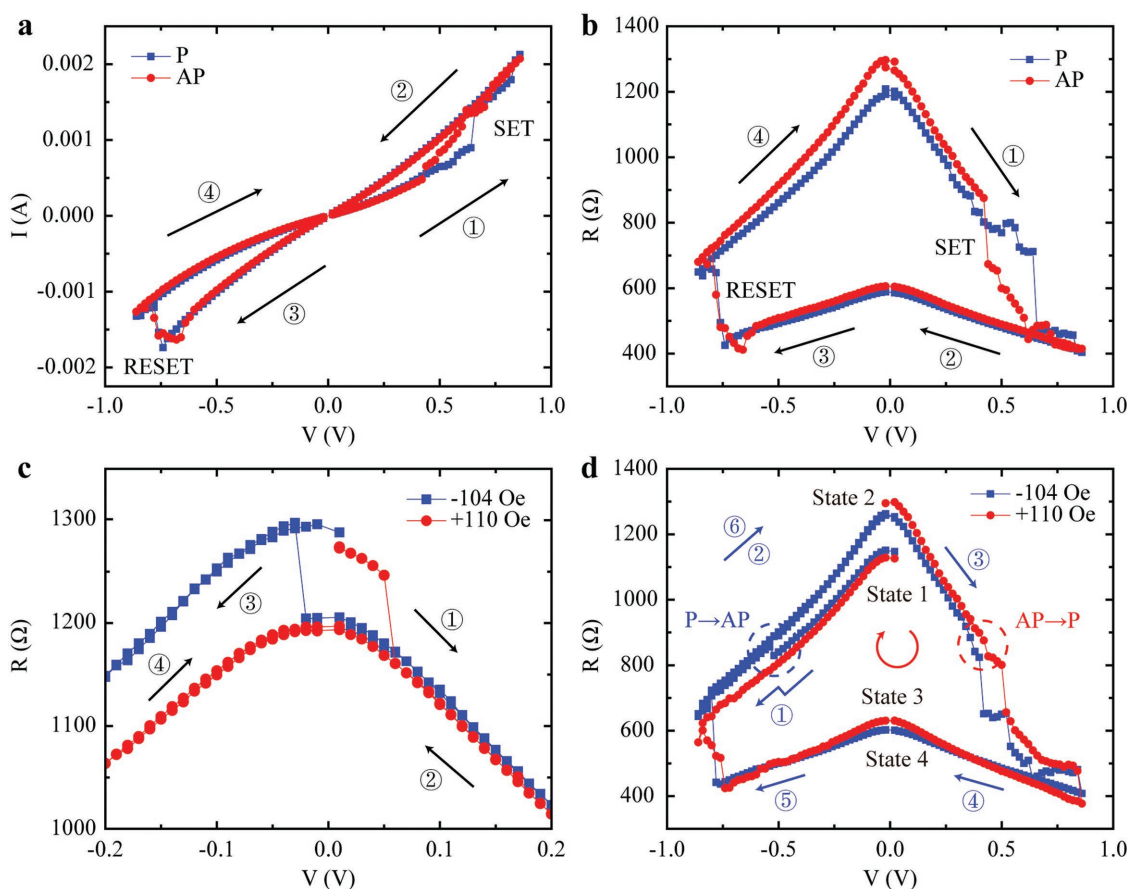
ADVANCED
SCIENCE NEWS
www.advancedsciencenews.com

ADVANCED
ELECTRONIC
MATERIALS
www.advelectronicmat.de

Figure 2. Transport properties of the Re-MTJ device. The direction of the external magnetic field is along the easy axis of the ellipse. The arrows and numbers (①–⑥) indicate the voltage sweep direction. States 1 to 4 correspond to the resistance states described in Figure 4b. a) I–V curves without an applied magneticfield up to ± 1 V. The MTJ was set to either the P or AP configuration before the measurement. The SET and RESET voltages are indicated. b) Corresponding R–V curves of (a). c) R–V curves under external positive and negative magnetic fields for voltages below ± 0.2 V, indicating pure CIMS without VIRS. d) R–V curves under external positive and negative magnetic fields up to ± 1 V. The VIRS process is observed near +0.5 V (SET) and −0.7 V (RESET). For the CIMS process, P to AP switching is observed near −0.5 V for a magnetic field of −104 Oe and near +0.4 V for a magnetic field of +110 Oe.

set to either the P or AP state using the external magnetic field before the measurement. Clear resistive switching behavior was observed from which the SET and RESET voltages could be identified. Figure 2b shows the corresponding R–V curve for the P and AP configurations, in which the low-resistance state (LRS) and high-resistance state (HRS) can be observed. Here, the LRS is ≈600 Ω, irrespective of the magnetic configurations, and the HRS is ≈1100 Ω and 1300 Ω for the P and AP states, respectively. We note that the low TMR (around 20%) presented here is related to a degraded crystalline structure of MgO layer with only 0.8 nm, for the facts that MgO(001) acts as a template to crystallize CoFe(B) and a bcc structure of CoFeB is crucial for gaining high TMR.[9] Since the MgO layer grown on an amorphous CoFeB is only expected to have highly oriented polycrystalline MgO(001) structure when t_{MgO} < 5ML (1.05 nm),[29] an optimization for TMR is possible for increasing the thickness of MgO layer. In this example, the typical ON/OFF ratio for the AP state was ≈120%, but ratios reaching 1000% were observed (see Figure S2 in the Supporting Information). Notably, magnetization switching between the P and AP states was not observed during the voltage sweep. Additionally, we observed that the SET and RESET voltages were independent of the magnetic

configuration. Figure 2c shows the R–V curve under the in-plane magnetic fields[30] that were used to assist CIMS. Pure CIMS was not obtained here at low voltages due to the thickness of the free layer. The maximum voltage applied was below 0.2 V in order to avoid VIRS and maintain the HRS. We observed CIMS assisted by the magnetic fields of $H_{ext}^{AP \to P} = +110$ Oe and $H_{ext}^{P \to AP} = -104$ Oe with typical current densities of $J_c^{AP \to P} = 1.7 \times 10^5$ A cm^{-2} and $J_c^{P \to AP} = 0.8 \times 10^5$ A cm^{-2}, respectively. These results show that CIMS and VIRS could be controlled independently. To observe both effects, a voltage was applied between ±0.8 V under a magnetic field (Figure 2d). In this case, we clearly observed that the VIRS and CIMS effects could act simultaneously.

The results shown in Figure 2 are different from those of previous findings involving RS due to the filamentary current path in the MgO barrier. First, in our experiment, we observed bipolar switching instead of unipolar switching (SET and RESET were caused by applying voltages with the same polarity). In addition, we observed both MS and RS in the same R–V loop; this result suggests two independent origins for the CIMS and RS processes. To gain more insight, we carefully investigated the microstructures of the elements. The nanofabrication

process of the device consisted of encapsulating the CoFe(B)-MgO nanopillars with a SiO$_x$ insulator in contact with the edges of the nanostructure (see Figures 1b and 3a). In the following, we provide evidence that the VIRS behavior was induced by the presence of the resistive Si filaments at the edges of the nanopillars. Microscopic structure characterizations were performed using energy-dispersive X-ray spectroscopy (EDS). **Figure 3**b,c indicates the presence of the Ta and Si elements detected by

measuring the characteristic peaks of the Ta-L$_\alpha$ (8.145 keV) and Si-K series lines, respectively. Note that since Ta-M$_\alpha$ (1.709 keV) and Si-K$_\alpha$ (1.739 keV) were separated by only 30 eV, the detector could not resolve these lines.[31,32] The detection results of both the Si and Ta elements overlapped, as seen in Figure 3c. Thus, the comparison between Figure 3b and Figure 3c clearly evidenced that Si aggregation occurred along the sidewall of the nanopillars with a typical width of 5–10 nm. In addition, the
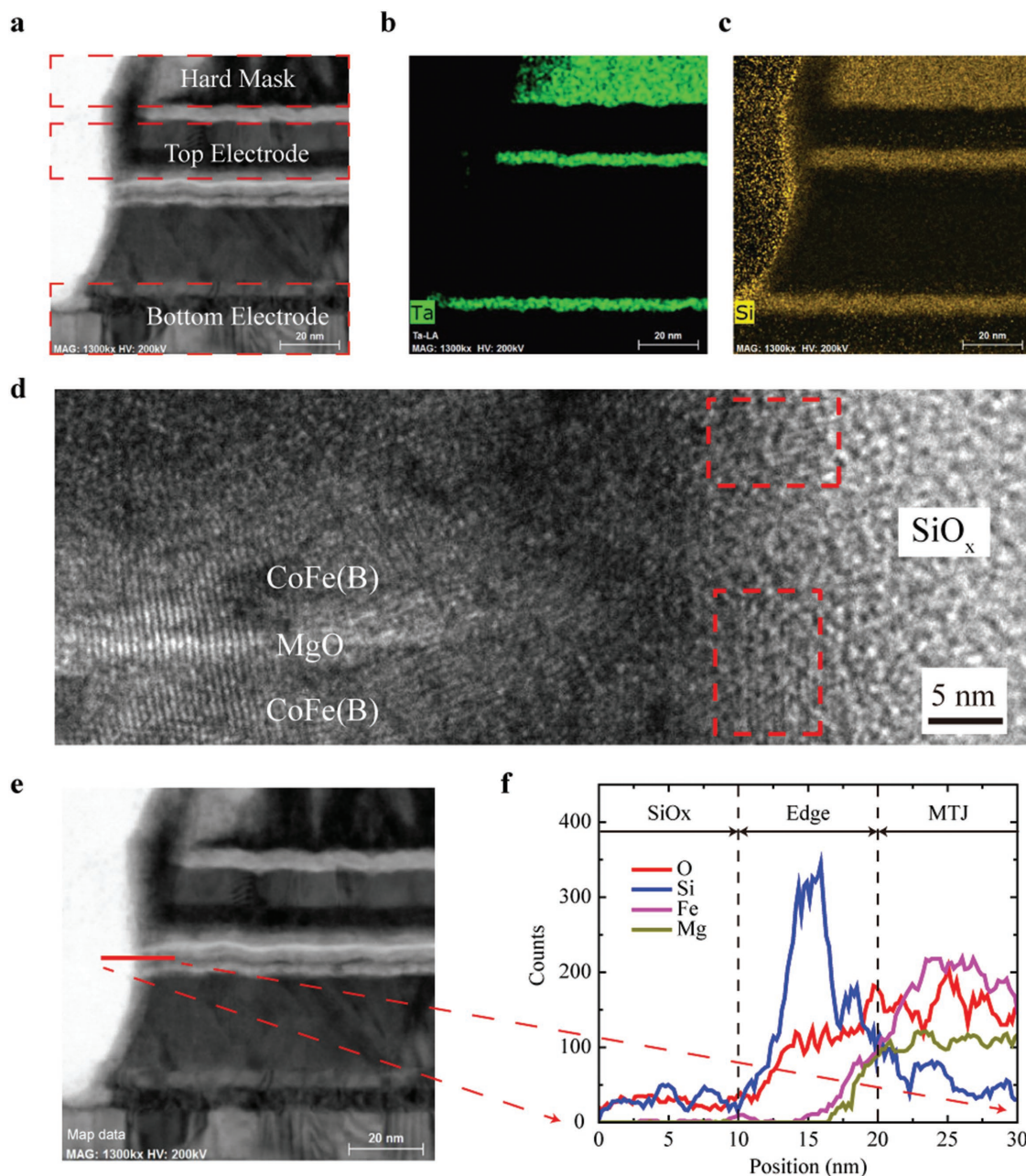

Figure 3. Microstructural characterization of the Re-MTJ device. a) Scanning TEM (STEM) image near the vertical edge of the MTJ nanopillar. The regions of the hard Ta mask, top electrode and bottom electrode, are indicated by the red dashed rectangles. b) EDS mapping of Ta using the Ta-L$_\alpha$ line characteristic peaks. c) EDS mapping of Si using the Si-K series line characteristic peaks. Note that since the Ta-M$_\alpha$ (1.709 keV) and Si-K$_\alpha$ (1.739 keV) peaks overlap, Ta is also detected. d) HRTEM image of the edges of the nanopillars. Nanocrystalline structures embedded in the SiO$_x$ matrix are indicated by the red dashed rectangles. e) STEM image obtained using a high-angle annular dark-field (HAADF) detector. The EDS linescan is marked in red and was measured from the SiO$_x$ matrix into the MTJ nanopillar. f) EDS linescans for O, Si, Fe, and Mg corresponding to the red line are indicated in (e). Three different regions can be delimited: a pure SiO$_x$ region, an intermixed layer with aggregates of Si and O (10 nm), and an MTJ region.

high-resolution TEM (HRTEM) images of the nanodevice indicate the presence of nanocrystals with a typical size of 5–10 nm embedded in the amorphous SiO_x along the edges of the nanopillars (see Figure 3d). The microstructural analysis and the electrical results of Figure 2 are consistent with the results from recent studies, which indicated that RS in a SiO_x matrix can be induced in the presence of embedded Si nanocrystals.[23,33–35] More precisely, when an SET voltage is applied, the Si nanocrystals can grow locally by favouring an electrochemical reduction process from $SiO_x \rightarrow Si$. This process induces a Si pathway (Si filaments) along the current flow direction, whereas a RESET voltage can favour the $Si \rightarrow SiO_x$ inverse process. This mechanism corresponds to a point-switching filament process involving local breakage and bridge evolution.

One important question is related to the presence of Si nanocrystals in our devices. It has been shown that the forming process of Si nanocrystals can be induced within pure SiO_x matrixes at low temperatures by etching the SiO_x.[23,36] In this case, the Si filaments can germinate at the edges of the SiO_x elements due to the presence of defects. In our case, the SiO_x matrix surrounding the nanopillars was obtained by spinning a polymer (Accuflo) and transforming it into an insulator using an annealing process at ≈300 °C. During the annealing process, the edges of the nanopillars involving damage induced by the etching process (see the Experimental Section and Note 6, Supporting Information) could serve as seed interfaces to nucleate the Si nanocrystals. In addition, the crystalline character of the MTJ may have also favored the germination of the Si nanocrystals. Indeed, an EDS linescan measured from the SiO_x matrix into the MgO barrier (see Figure 3e,f) indicated that both Si and O aggregated at the edges of the nanopillars on a scale of 10 nm with a ratio of silicon to oxygen elements that was much higher at the edges than in the SiO_x matrix. The fact that bipolar behavior was observed here for the SET and RESET processes may have been related to the presence of mobile oxygen ions.

Based on the analyses described above, a proposed schematic of the Re-MTJ device is presented in **Figure 4**a that consists of an MTJ-based element connected in parallel with a Si filament element. Such a device structure indicates that four distinct configurations with different resistance states can be achieved (see Figure 4b); this result is in agreement with the experimental
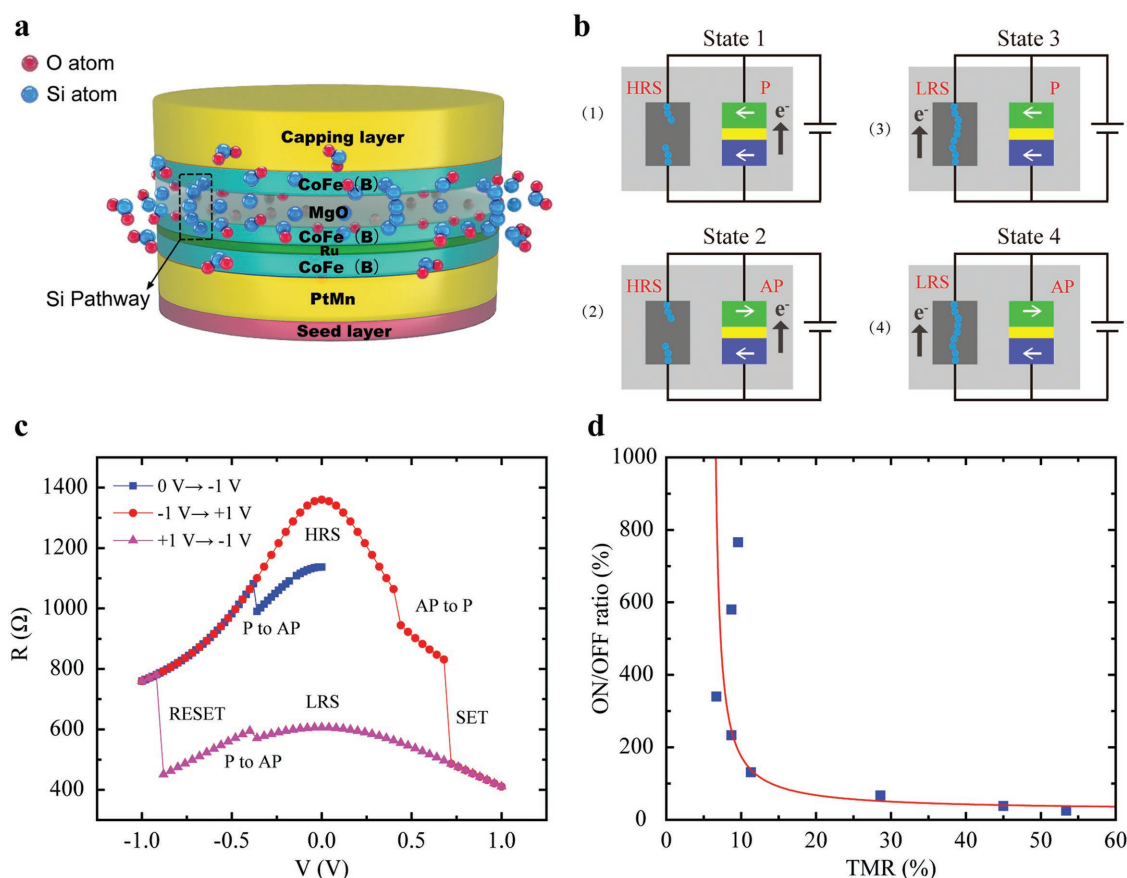

Figure 4. Resistance switching model of the Re-MTJ device. a) Schematic of the MTJ nanopillar surrounded by Si filaments. The blue and red balls represent the Si atoms and O atoms, respectively. b) Physical model corresponding to an RRAM element in parallel with an MRAM element. Depending on the configuration of the RRAM and MRAM elements, four different states can be obtained in the Re-MTJ device. The blue balls represent the conductive filaments that form the Si pathway. States 1–4 correspond to those in Figure 2d. c) Simulation of the R–V behavior using a compact model of STT-MTJ and an MIM resistive junction connected in parallel. A magnetic field was not included in the simulation. d) Relationship between the ON/OFF ratio and the TMR ratio measured from the different devices. The TMR was obtained through R–H measurements under a low voltage of 10 mV. The ON/OFF ratio was obtained after conducting a voltage (current) sweep. The blue squares are the experimental data, and the red line is a guide for the eyes.
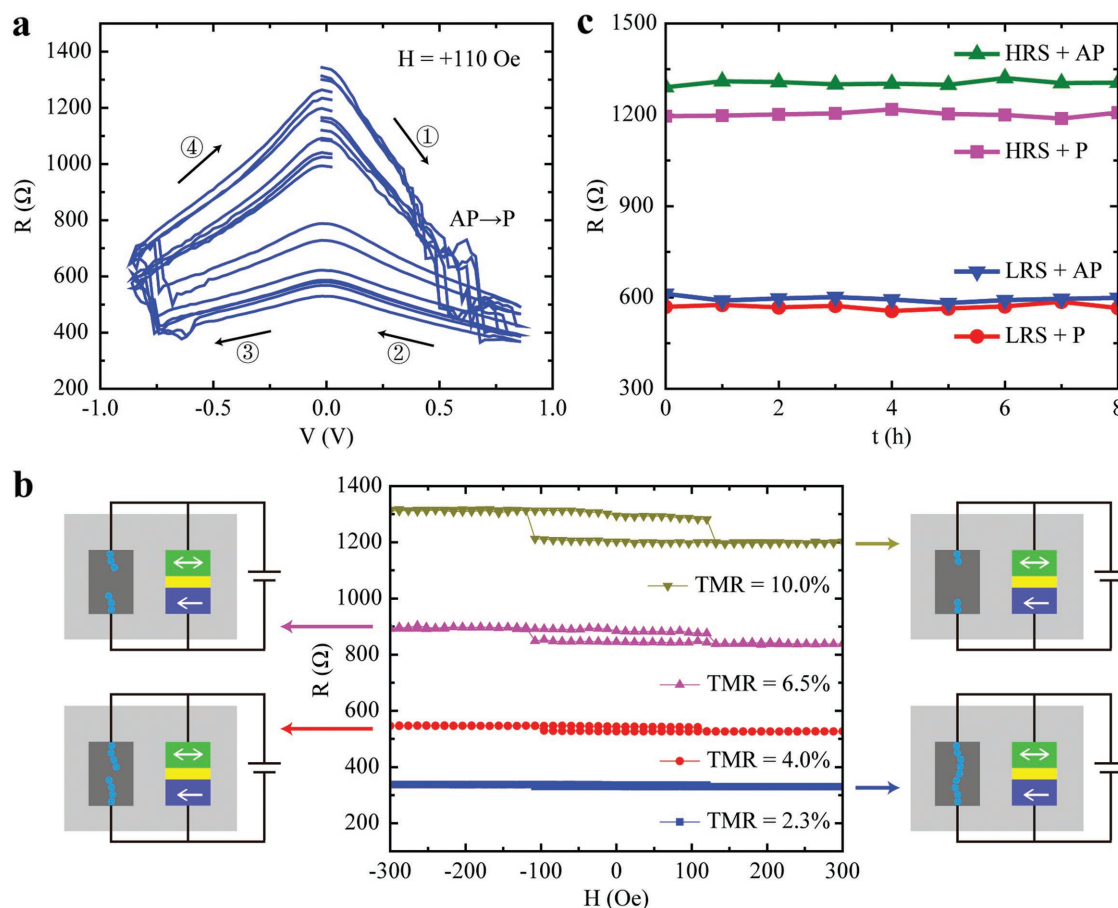
Figure 5. Multilevel resistance states in the Re-MTJ device. a) Seven different R–V curves under external magnetic fields in the same device. b) R–H hysteresis loops with different initial resistance states for the same device. The measurements were conducted from an LRS (≈600 Ω) to an HRS (≈1300 Ω). c) Time-independent resistance curves showing the nonvolatile features of the Re-MTJ for four different resistance states (LRS+AP, LRS+P, HRS+AP, and HRS+P).

results (see Figure 2d). When the Si filaments are not conductive (RESET process), the current mainly goes through the MTJ, resulting in an HRS, and when the Si filaments becomes conductive (SET process), the current mainly flows through the Si filaments, resulting in an LRS. To further verify the proposed device model, simulations were performed using a compact model that integrated a physical-based spin-transfer-torque (STT)-MTJ[37] and a bipolar metal–insulator–metal (MIM) resistive junction[38] connected in parallel (see Figure 4c). Using the parameters of R_{AP} = 1390 Ω, R_P = 1160 Ω, R_{HRS} = 64 500 Ω, and R_{LRS} = 660 Ω, the R–V curve of Figure 2d that combines the features of CIMS and VIRS could be well reproduced. Furthermore, another interesting feature related to the microstructural properties of the devices is the strong correlation between the ON/OFF ratio of the RS and the TMR value of the MS (see Figure 4d). In particular, the ON/OFF ratio increased when the TMR value was reduced. This result suggests that when the TMR ratio was low, a point-switching filament process could occur, whereas when the TMR was higher, the conduction through the Si filaments was not active. Notably, the ON/OFF ratio and TMR behavior in these devices originated from the formation of an

Si pathway in the SiO_x matrix[23] and the Δ_1 Bloch states filtering at the CoFe(B)/MgO interface,[39] respectively. The oxygen ion movement from the SiO_x matrix toward the MTJ nanopillars promoted the nucleation of the Si nanocrystals and affected the Fe—O bonds at the CoFe(B)/MgO interface;[28,39–41] these processes resulted in a high ON/OFF ratio but a low TMR. As a result, the mobile oxygen ions near the edges of the nanopillars (see Figure 4a) played a joint role in both the ON/OFF ratio and the TMR value.

The multilevel states of the Re-MTJ device were investigated and are presented in **Figure 5**. Figure 5a shows seven consecutive R–V curves indicating that different resistance states could be reached using a single device. Each R–V curve corresponds to a different degree of the Si oxidation pathway, and the pathways were randomly induced by the combination of a local strong electric field and heating during the point-switching filament process. Figure 5b presents a Re-MTJ device that exhibited eight different states by combining two magnetic states (P and AP) with four different resistance states of the Si filaments. A larger TMR ratio was achieved for higher resistance states; this result reflects that the lower resistance of the MTJ

dominated the current pathway. Furthermore, the data retention of the Re-MTJ device was tested for four different resistance states (see Figure 5c). All the configurations exhibited robust nonvolatile properties. Although the resistances between LRS with P and LRS with AP are close (see Figure S5 in the Supporting Information), it can be improved by enhancing the TMR ratio with the further optimization of fabrication process.

3. Conclusion

In conclusion, we fabricated a heterogeneous memristive device, Re-MTJ, an advanced NVM device that combines the merits of MRAM and RRAM. The Re-MTJ device integrates an MTJ nanopillar encapsulated by a SiO_x-based polymer with surrounding resistive silicon filaments. We observed both MS and RS in the Re-MTJ; these behaviors originated from the MTJ and silicon filaments, respectively. We reported a rather high ON/OFF ratio and multilevel resistance behavior owing to the point-switching silicon filament process. These properties are rather preferable for high-reliability and high-density memory applications. The presence of nanocrystals within the silicon aggregates was confirmed by the microscopic structure characterizations. The proof-of-concept demonstration here involved low TMR values, but in principle, our approach can enable one to independently optimize the properties of the MTJ and silicon elements. The Re-MTJ device, with the merits of a high ON/OFF ratio, long endurance, and multilevel resistance behavior, can certainly benefit the advancement of memristive memory and computing architectures, such as in-memory computing and neuromorphics.

4. Experimental Section

Sample Preparation: The magnetic multilayers were deposited onto SiO_2-coated Si wafers using a combination of radio frequency (RF) and direct current (DC) sputtering in a Canon Anelva system. From the substrate side, the MTJ structure consisted of the following layers: Ta(5)/Ru(15)/Ta(5)/Ru(15)/Ta(5)/Ru(5)/PtMn(20)/CoFeB(1.5)/CoFe(2.0)/Ru(0.85)/CoFeB(1.5)/CoFe(1.5)/MgO(0.8)/CoFe(1.5)/CoFeB(1.5)/Ru(2)/Ta(5)/Ru(10) (the numbers are the nominal thicknesses in nanometers). The bottom and top layers, Ta(5 nm)/Ru(15 nm)/Ta(5 nm)/Ru(15 nm)/Ta(5 nm)/Ru(5 nm) and Ru(2 nm)/Ta(5 nm)/Ru(10 nm), respectively, were designed for the current-in-plane tunneling (CIPT) measurements using a CAPRES microprobe tool. The typical TMR ratio and the resistive-area product of the unpatterned films were ≈144% and ≈ 19 Ω μm^2, respectively. Then, the annealing was performed at 350 °C for 1 h with an in-plane applied magnetic field of 1 T under a vacuum of 10^{-6} Torr. After the deposition, the multilayers were patterned into submicrometer-sized ellipses by electron beam lithography and ion beam etching. A low-temperature curing process of Accuflo was utilized for encapsulating the patterned structure.

Transport Measurements: The fabricated devices were characterized using dc-transport measurements under in-plane magnetic fields (with a precision below 1×10^{-3} Oe) with a two-probe geometry at room temperature. A bias voltage (or current) was applied to the top electrode, while the bottom electrode was grounded. The voltage–pulse (or current–pulse) durations were $\tau_p = 200$ ms, and the remanent resistance of the Re-MTJ device was measured under a low bias between each voltage (or current) change.

Model Simulation: The compact model of the device was written using Verilog-A language and evaluated in a Cadence Spectre environment. The compact model integrated a physical-based STT-MTJ and a bipolar MIM resistive junction connected in parallel. Magnetic fields were not considered in the simulation.

Supporting Information

Supporting Information is available from the Wiley Online Library or from the author.

Conflict of Interest

The authors declare no conflict of interest.

[1] E. Linn, R. Rosezin, S. Tappertzhofen, U. Böttger, R. Waser, *Nanotechnology* **2012**, *23*, 305205.
[2] J. J. Yang, D. B. Strukov, D. R. Stewart, *Nat. Nanotechnol.* **2013**, *8*, 13.
[3] H. S. P. Wong, S. Salahuddin, *Nat. Nanotechnol.* **2015**, *10*, 191.
[4] J. Borghetti, G. S. Snider, P. J. Kuekes, J. J. Yang, D. R. Stewart, R. S. Williams, *Nature* **2010**, *464*, 873.
[5] M. M. Shulaker, G. Hills, R. S. Park, R. T. Howe, K. Saraswat, H.-S. P. Wong, S. Mitra, *Nature* **2017**, *547*, 74.
[6] N. Locatelli, V. Cros, J. Grollier, *Nat. Mater.* **2013**, *13*, 11.
[7] J. Grollier, D. Querlioz, M. D. Stiles, *Proc. IEEE* **2016**, *104*, 2024.
[8] M. Prezioso, F. Merrikh-Bayat, B. D. Hoskins, G. C. Adam, K. K. Likharev, D. B. Strukov, *Nature* **2015**, *521*, 61.
[9] S. Yuasa, D. D. Djayaprawira, *J. Phys. D: Appl. Phys.* **2007**, *40*, R337.
[10] S. Ikeda, K. Miura, H. Yamamoto, K. Mizunuma, H. D. Gan, M. Endo, S. Kanai, J. Hayakawa, F. Matsukura, H. Ohno, *Nat. Mater.* **2010**, *9*, 721.
[11] A. D. Kent, D. C. Worledge, *Nat. Nanotechnol.* **2015**, *10*, 187.
[12] H. S. P. Wong, H. Y. Lee, S. Yu, Y. S. Chen, Y. Wu, P. S. Chen, B. Lee, F. T. Chen, M. J. Tsai, *Proc. IEEE* **2012**, *100*, 1951.
[13] W. Lin, S. Liu, T. Gong, Q. Zhao, W. Huang, *Adv. Mater.* **2014**, *26*, 570.
[14] U. Celano, L. Goux, A. Belmonte, K. Opsomer, A. Franquet, A. Schulze, C. Detavernier, O. Richard, H. Bender, M. Jurczak, W. Vandervorst, *Nano Lett.* **2014**, *14*, 2401.
[15] D. Querlioz, O. Bichler, A. F. Vincent, C. Gamrat, *Proc. IEEE* **2015**, *103*, 1398.
[16] D. Zhang, L. Zeng, K. Cao, M. Wang, S. Peng, Y. Zhang, Y. Zhang, J. O. Klein, Y. Wang, W. Zhao, *IEEE Trans. Biomed. Circuits Syst.* **2016**, *10*, 828.

[17] Y. J. Song, J. H. Lee, H. C. Shin, K. H. Lee, K. Suh, J. R. Kang, S. S. Pyo, H. T. Jung, S. H. Hwang, G. H. Koh, in *Electron Devices Meeting (IEDM)*, IEEE, Piscataway, NJ **2016**, pp. 27.2.1–27.2.4.

[18] N. Tezuka, S. Oikawa, I. Abe, M. Matsuura, S. Sugimoto, K. Nishimura, T. Seino, *IEEE Magn. Lett.* **2016**, *7*, 3104204.

[19] W. Kang, Z. Li, J. Klein, Y. Chen, Y. Zhang, D. Ravelosona, C. Chappert, W. Zhao, *IEEE Trans. Nanotechnol.* **2014**, *13*, 1088.

[20] D. Halley, H. Majjad, M. Bowen, N. Najjari, Y. Henry, C. Ulhaq-Bouillet, W. Weber, G. Bertoni, J. Verbeeck, G. Van Tendeloo, *Appl. Phys. Lett.* **2008**, *92*, 212115.

[21] P. Krzysteczko, G. Reiss, A. Thomas, *Appl. Phys. Lett.* **2009**, *95*, 112508.

[22] J. M. Teixeira, J. Ventura, R. Fermento, J. P. Araujo, J. B. Sousa, P. Wisniowski, P. P. Freitas, *J. Phys. D: Appl. Phys.* **2009**, *42*, 105407.

[23] J. Yao, Z. Sun, L. Zhong, D. Natelson, J. M. Tour, *Nano Lett.* **2010**, *10*, 4105.

[24] J. Chen, C. Huang, C. Chiu, Y. Huang, W. Wu, *Adv. Mater.* **2015**, *27*, 5028.

[25] S. Kumar, C. E. Graves, J. P. Strachan, E. M. Grafals, A. L. D. Kilcoyne, T. Tyliszczak, J. N. Weker, Y. Nishi, R. S. Williams, *Adv. Mater.* **2016**, *28*, 2772.

[26] C. Li, B. Gao, Y. Yao, X. Guan, X. Shen, Y. Wang, P. Huang, L. Liu, X. Liu, J. Li, C. Gu, J. Kang, R. Yu, *Adv. Mater.* **2017**, *29*, 1602976.

[27] W. Huang, J. Kennedy, R. Katsanes (Honeywell), *U.S. Patent 7, 910,223*, **2011**.

[28] Z. Wang, M. Saito, K. P. McKenna, S. Fukami, H. Sato, S. Ikeda, H. Ohno, Y. Ikuhara, *Nano Lett.* **2016**, *16*, 1530.

[29] S. Yuasa, Y. Suzuki, T. Katayama, K. Ando, *Appl. Phys. Lett.* **2005**, *87*, 242503.

[30] X. Lou, Z. Gao, D. V. Dimitrov, M. X. Tang, *Appl. Phys. Lett.* **2008**, *93*, 242502.

[31] C. D. Wagner, L. H. Gale, R. H. Raymond, *Anal. Chem.* **1979**, *51*, 466.

[32] C. Hollerith, D. Wernicke, M. Bühler, F. v. Feilitzsch, M. Huber, J. Höhne, T. Hertrich, J. Jochum, K. Phelan, M. Stark, B. Simmnacher, W. Weiland, W. Westphal, *Nucl. Instrum. Methods Phys. Res., Sect. A* **2004**, *520*, 606.

[33] J. Yao, L. Zhong, D. Natelson, J. M. Tour, *Appl. Phys. A* **2011**, *102*, 835.

[34] G. Xia, Z. Ma, X. Jiang, H. Yang, J. Xu, L. Xu, W. Li, K. Chen, D. Feng, *J. Non-Cryst. Solids* **2012**, *358*, 2348.

[35] Y. Wang, X. Qian, K. Chen, Z. Fang, W. Li, J. Xu, *Appl. Phys. Lett.* **2013**, *102*, 042103.

[36] F. Zhou, Y. F. Chang, Y. Wang, Y. T. Chen, F. Xue, B. W. Fowler, J. C. Lee, *Appl. Phys. Lett.* **2014**, *105*, 163506.

[37] Y. Zhang, W. Zhao, Y. Lakys, J. O. Klein, J. Von Kim, D. Ravelosona, C. Chappert, *IEEE Trans. Electron Devices* **2012**, *59*, 819.

[38] U. Russo, D. Ielmini, C. Cagli, A. L. Lacaita, *IEEE Trans. Electron Devices* **2009**, *56*, 193.

[39] X.-G. Zhang, W. H. Butler, A. Bandyopadhyay, *Phys. Rev. B* **2003**, *68*, 092402.

[40] C. Tusche, H. L. Meyerheim, N. Jedrecy, G. Renaud, A. Ernst, J. Henk, P. Bruno, J. Kirschner, *Phys. Rev. Lett.* **2005**, *95*, 176101.

[41] F. Bonell, S. Andrieu, A. M. Bataille, C. Tiusan, G. Lengaigne, *Phys. Rev. B: Condens. Matter Mater. Phys.* **2009**, *79*, 224405.